OPTIMIZATION OF THE AUTOMOTIVE AIR CONDITIONING SYSTEM USING RADIAL BASIS FUNCTION NEURAL NETWORK

by

Pingqing FAN**, Xipei MA, Yong CHEN, Tao YUAN, and Tianhong LIU

School of Mechanical and Automotive Engineering,
Shanghai University of Engineering Science, Shanghai, China

Original scientific paper
https://doi.org/10.2298/TSCI210225280F

The defrosting performance of automotive air conditioners plays an important role in driving safety. This paper uses CFD to simulate the internal flow field of the automobile numerically. Simulation results show that the flow distribution is unreasonable. The horizontal grilles are added at the outlets to improve the defrosting performance of the automobile. Air-flow jet angle and the length of the air conditioning outlets (L_1, L_2) are selected as design variables based on the radial basis neural network to find the optimal combination scheme. The area of the defrosting dead corner has been reduced from 20-5% after optimization, and the frost layer of the front windshield has been completely melted in 25 minutes. The experiment test is conducted to verify the improvement of the defrosting performance of automotive air conditioners. The design methodology can be applied to the development of the air conditioner.

Key words: *defrosting performance, automotive air conditioning, optimization, radial basis neural network*

Introduction

Frosting and fogging of automobile windshields is a practical problem frequently encountered in the course of driving [1]. The defrosting performance of the front windshield affects the safety of drivers and passengers. Therefore, effectively improving the defrosting performance of automobile air conditioning systems has become a serious problem in the auto industry [2-4]. With the development of computer techniques, the CFD technique has been widely used in the optimization research of defrosting performance [5, 6].

A considerable amount of research has been conducted in this area in the past years. Ikeda *et al.* [7] simulated the air-flow from the inlet of the air conditioner and compared their results with the experimental findings to verify the feasibility of CFD numerical analysis. Aroussi *et al.* [8] simulated the defrosting process of the vehicle side window and indicated the insufficient design of the experimental vehicle defrosting system. Swales *et al.* [9] described how to combine usage of CAE with a newly developed laser based technique and provided an excellent method for maximising defrost and demist performance. Kang *et al.* [10] studied the automotive defrosting system and verified the simulation results. They found that the air-flow from the outlet is not uniform and does not cover the entire windshield area, thus affecting the defrosting efficiency. Karim *et al.* [11] found that the structural adjustment of defrosting ducts can improve

* Corresponding author, e-mail: fanpingqing@163.com

the defrosting performance of vehicle windshields. Huang *et al.* [12] improved the internal structure of the defroster duct to improve the defrost effect. Li *et al.* [13] used the resistance wire heating method to accelerate the defrosting of the bus air conditioner due to insufficient heat source, which affects the defrosting effect of the windshield. However, optimizations of the model are based on working experience. The optimization method is slightly inefficient and blind. Moreover, obtaining the best results is difficult using this method.

In recent years, response surface methodology (RSM) has been employed in many design fields. For example, Yang *et al.* [14] used RSM to optimize the centrifugal fan and reduce automobile noise. However, RSM also has certain limitations. Cho *et al.* [15] believed that RSM is best for two or fewer design variables, and optimizing multiple design variables simultaneously is difficult. In most cases, the object that must be modeled is a complex large system, and no explicit mathematical expression exists between the design variables and the target. Neural networks can capture the non-linear relationship between variables and the target and solve the optimization problem of multiple design variables. Some researchers have successfully applied neural networks to optimization with multiple variables. Atuanya *et al.* [16] used neural networks to predict the mechanical properties of palm wood fiber-recycled low density polyethylene composite. Selvan [17] and Esonye *et al.* [18] used RSM and neural networks to model the optimization with multiple variables and found that the neural network has a high modelling accuracy for the optimization with more than three variables. The neural networks introduce improved results for the optimization with multiple variables.

Radial basis function neural network principle

The neural network is a mathematical model that imitates the behavior of the biological neural network and performs the distributed parallel information processing. The neural network comprises many neurons that are connected. The structure of the neural network is changed in accordance with the input information. The modelling process mainly adjusts the weights between neurons. Up to now, the types of neural network models are quite rich and have developed to nearly 40 kinds [19, 20]. Among the many networks, radial basis function neural network (RBFNN) has the advantages of simple structure and solid mathematical foundation, thus, this network is widely used in many fields.

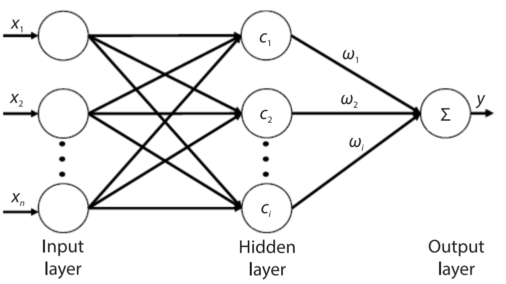

Figure 1. Structure of RBFNN

The structure of the RBFNN is a three-layer forward network, (fig. 1, which includes input, hidden, and output layers. The first layer is the input layer, which comprises the signal source node. This layer only serves to transmit signals and the second layer is the hidden layer, and the number of hidden layer nodes is determined by the problem described. The transformation function (radial basis function) of neurons in the hidden layer, as a local response function, is a non-negative linear function with radial symmetry and attenuation the center point. The third layer is the output layer, which responds to the input [21, 22].

The Gaussian function is commonly used as the activation function of RBFNN. The expression of the Gaussian function is presented:

$$R\left(x_p - c_i\right) = \exp\left(-\frac{1}{\delta_i^2}\left\|x_p - c_i\right\|^2\right), \quad p = 1,2,\cdots,n, \quad i = 1,2,\cdots,m \tag{1}$$

where $R(x_p - c_i)$ is the output of i^{th} hidden layer node, $||x_p - c_i||^2$ – the Euclidean norm, x_p – the p^{th} input sample, c_i – the i^{th} Gaussian function center of the hidden layer, δ_i – the variance of the i^{th} Gaussian function, which is also called the width or expansion constant of the Gaussian function, m – the number of hidden layer nodes, and n – the number of hidden layer nodes.

The output layer has only one node, which is the prediction result. The output can be expressed as shown:

$$y_p = \sum_{i=1}^{m} \omega_i R\left(x_p - c_i\right) + b_i, \quad p = 1,2,\cdots,n, \quad i = 1,2,\cdots,m \tag{2}$$

where ω_i is the weight of the hidden layer to the output layer and b_i – the bias term.

Topology analysis

Mathematical models of defrosting

The realizable k-ε turbulence model [23] was adopted in the article, which can simulate rotary shear flow, free flow and submerged water jet well, as well as the velocity and direction of air-flow generated in the flow field. Its governing equations are given:

$$\frac{\partial(\rho k)}{\partial t} + \frac{\partial(\rho k u_i)}{\partial x_i} = \frac{\partial}{\partial x_j}\left[\left(\mu_1 + \frac{\mu_t}{\sigma_k}\right)\frac{\partial k}{\partial x_j}\right] + G_k + G_\mathrm{b} - \rho\varepsilon - Y_M + S_k \tag{3}$$

$$\frac{\partial(\rho\varepsilon)}{\partial t} + \frac{\partial(\rho\varepsilon u_i)}{\partial x_i} = \frac{\partial}{\partial x_j}\left[\left(\mu_1 + \frac{\mu_t}{\sigma_\varepsilon}\right)\frac{\partial\varepsilon}{\partial x_j}\right] + \rho C_{1\varepsilon}\varepsilon - \rho C_{2\varepsilon}\frac{\varepsilon^2}{k + \sqrt{u\varepsilon}} + C_{1\varepsilon}\frac{\varepsilon}{k}C_{3\varepsilon}G_b + S_\varepsilon \tag{4}$$

where k is turbulent kinetic energy, ε – the turbulent dissipation rate, ρ – the air-flow density, x_i, x_j – are the position vectors, u_i – the velocity, μ_t – the turbulent viscosity coefficient, μ_1 – the molecular viscosity, σ_k, σ_ε – the turbulent Prandtl number of turbulent kinetic energy and turbulent dissipation rate, which are 1.0 and 1.3, respectively, G_k – the turbulent kinetic energy caused by average velocity gradient, G_b – the turbulent kinetic energy caused by buoyancy, Y_M – the contribution of compressible velocity turbulent pulsation expansione, $C_{1\varepsilon}$, $C_{2\varepsilon}$, and $C_{3\varepsilon}$ are constants, and S_k, S_ε are user-defined source items.

The defrosting of automobile windshield is the melting process of frost layer under the hot air-flow and the energy equation can be expressed:

$$\frac{\partial}{\partial t}(\rho H) + \nabla(\rho\vec{\mathrm{v}}H) = \nabla(k\nabla T) + S \tag{5}$$

where H is the enthalpy, $\vec{\mathrm{v}}$ – the fluid velocity, and S – the active phase shown

$$S = \frac{\left(1-\beta^2\right)}{\left(\beta^3 + \sigma\right)} A_\mathrm{mush}\left(\vec{\mathrm{v}} - \vec{\mathrm{v}}_p\right) \tag{6}$$

where $\sigma = 0.001$ to avoid a denominator of 0, $A_\mathrm{mush} = 10^5$, $\vec{\mathrm{v}}_P$ – the velocity of ice-water mixture, β – the liquidus fraction. The $\beta = 0$ when the frost temperature, T, is lower than the solidus temperature T_solidus, $\beta = 1$ when T is higher than the liquid temperature T_liquidus, when T is between T_solidus and T_liquidus, $\beta = (T - T_\mathrm{solidus})/(T_\mathrm{liquidus} - T_\mathrm{solidus})$.

Numerical simulation

Figure 2 shows the simulation model of the automobile. The model includes a cabin, a glass layer, a frost layer, a defrosting duct, and a seat. The front windshield is divided into A, A', and B areas [24].

The entire computational domain is divided by tetrahedral meshes. The mesh is refined near the defroster duct and the frost and glass layers. The glass and frost layers each have five layers [25], as shown in fig. 3.

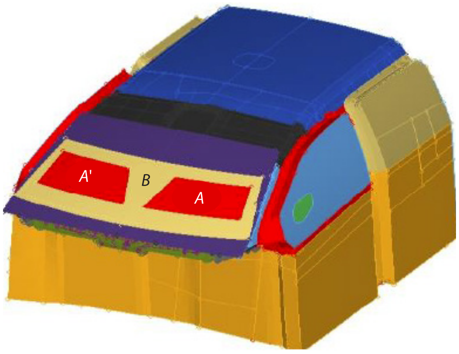

Figure 2. Physical model of the automobile

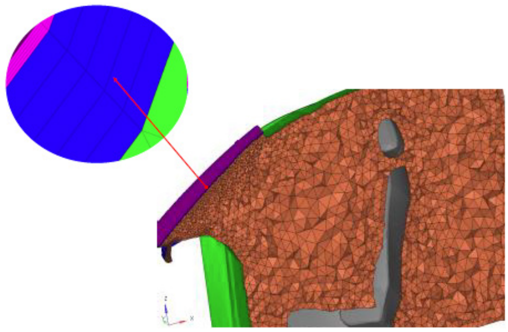

Figure 3. Grids of simulation domain

The air-flow is assumed to be incompressible and the environmental pressure is standard atmosphere. The inlet and outlet are set as mass-flow inlet and pressure outlet, respectively. The air temperature changes with time, the initial temperature is –18 °C, and the final temperature is 47.3 °C.

The ANSYS FLUENT software was used for CFD modelling and solution [26]. Simple algorithm in pressure-velocity coupling is adopted as the solution method and the second-order upwind difference scheme is used in the discrete differential algorithm. During the solutions, the convergence precision of the continuity and momentum equations are within 10^{-4}, and that of the energy equation is less than 10^{-5}.

Table 1 shows the flow distribution of each outlet after computation convergence. The flow rate of the driver's side outlet accounts for 10.96% and that of the passenger side is 11.04%; the flow distribution of the two outlets is reasonable. The flow rate of the central outlet accounts for 38.56%, the left side outlet is 19.44%, and the right outlet is 20%. The flow rate of the central outlet is approximately the sum of the left and right outlets, and the flow distribution of the three outlets are unreasonable.

Table 1. Flow distribution of each outlet

	Flow rate [kgs^{-1}]	Percentage [%]
Left outlet	0.0243	19.44
Central outlet	0.0482	38.56
Right outlet	0.0250	20.00
Driver-side outlet	0.0137	10.96
Passenger-side outlet	0.0138	11.04
Total	0.125	100

Topological improvements

Figure 4 shows the defrosting duct structure. The left, central, and right outlets are responsible for the defrosting operation of the front windshield. The driver- and passenger-side outlets are responsible for the side windshields.

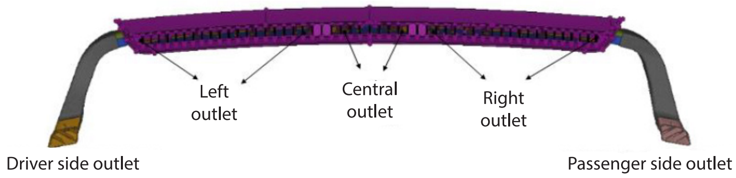

Figure 4. Defrosting duct structure and outlet position

The structural topology scheme aims to add horizontal grilles at the outlets, as shown in fig. 5. The horizontal grille can increase the resistance in the defrosting duct and squeeze the air-flow of the central outlet to the left and right outlets, thus resulting in reasonable flow distribution. The horizontal grille also helps the even distribution of air-flow over the windshield to improve defrosting efficiency.

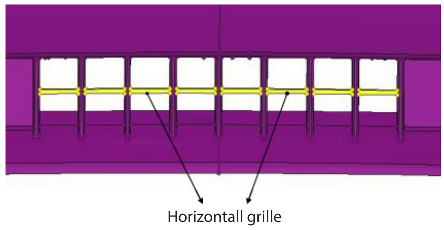

Figure 5. Topological improvements

Optimization Based on RBFNN

Design strategies

The RBFNN is used for the optimization of the air conditioning structure to improve the defrosting performance of the automobile. Figure 6 shows the optimization process.

The air-flow velocity on the A, A', and B areas of the front windshield f is chosen as the optimization objective. The optimization objective can be expressed as shown in eq. (7).

$$Maxf = \omega_1 v_A + \omega_2 v_{A'} + \omega_3 v_B \tag{7}$$

where v_A, $v_{A'}$, and v_B are, respectively surface weighted average air-flow velocity of the A, A', and B areas. The ω_1, ω_2, and ω_3 are weight coefficients. The defrosting work in A area was completed first, followed by the A', and the B areas. Thus, ω_1, ω_2, and ω_3 are, respectively set to 0.5, 0.3, and 0.2.

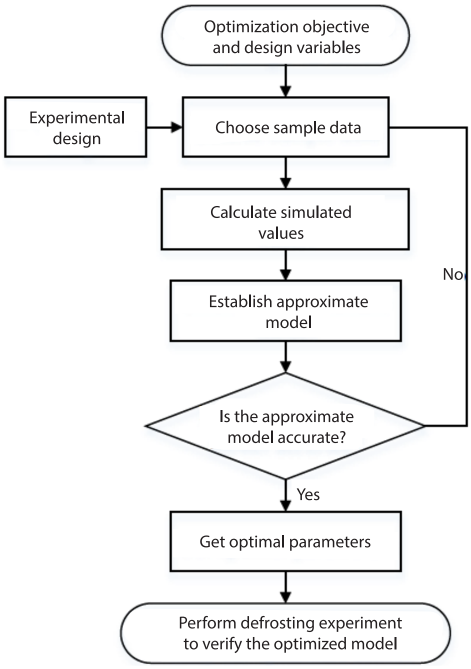

Figure 6. Optimization process

The length of the left and right outlets is the same due to the structural symmetry of the left and right outlets. The lengths of the left outlet, L_1, and the central outlet, L_2, and the air-flow jet angle, α, are chosen as design variables. The range of values of L_1, L_2, and α is 170 mm $\leq L_1 \leq$ 350 mm, 0 mm $\leq L_2 \leq$ 150 mm, and $0° \leq \alpha \leq 90°$, respectively. Thirty groups of analytic models are created using the Latin hypercube sampling method for the selection of sample points. The concrete parameters of each group and the final simulated values are presented in tab. 2.

Table 2. Concrete parameters and final values in each group

Groups	Design variables			Simulated value	Predicted value
	L_1 [mm]	L_2 [mm]	α [°]	f [ms^{-1}]	
1	255	17	89	2.918	1.978
2	204	51	71	3.490	3.428
3	170	102	58	3.447	3.375
4	238	34	28	3.430	3.501
5	221	68	32	3.216	3.287
6	340	119	13	4.156	4.138
7	187	17	11	3.879	3.743
8	170	51	82	4.045	3.123
9	187	68	23	3.612	3.702
10	306	34	7	3.192	2.808
11	221	85	36	3.129	2.959
12	272	68	2	3.090	3.317
13	238	119	73	3.160	2.642
14	323	68	55	3.637	3.450
15	306	0	86	1.25	2.643
16	204	85	34	3.308	3.316
17	255	85	52	3.255	2.552
18	238	102	20	3.179	3.266
19	204	34	45	3.301	4.147
20	187	51	66	3.984	3.892
21	289	85	48	3.979	2.895
22	306	17	46	2.756	2.869
23	238	136	41	3.249	3.325
24	340	136	63	3.904	4.596
25	272	119	77	3.223	3.157
26	323	119	3	4.071	4.098
27	323	17	79	3.227	3.402
28	255	17	16	2.879	3.490
29	289	85	62	3.493	3.007
30	289	119	26	4.009	3.820

Approximate model construction

An approximate model was constructed by RBFNN. First, the 30 sets of sample points are merged into a data set, where L_1, L_2, and α are independent input parameters. The approximate model generated a related parameter, that is, the air-flow velocity on the front windshield A, A', and B areas. The accuracy of the approximation model is verified by the coefficient of determination, R^2, and correction factor, R^2_{adj}. The coefficient of determination, R^2, measures the predicted value of the sample on the total variation proportion of the average value $\overline{y}$. The ideal model is one that can reflect all variabilities. The R^2 is a number between 1 and 0. The analytic model will be improved when the number is close to 1. The model is considered sufficiently good to be accepted when R^2 is between 0.95 and 1. The model is considered and then checked further with the modified R^2_{adj} when the number is between 0.9 and 0.95. The formulas for R^2 and R^2_{adj} are, respectively presented:

$$R^2 = \frac{\sum_{i=1}^{n}\left(\hat{y}-\overline{y}\right)^2}{\sum_{i=1}^{n}\left(y_i-\overline{y}\right)^2} \tag{8}$$

$$R^2_{\mathrm{adj}} = 1-\frac{N-1}{N-k-1}\left(1-R^2\right) \tag{9}$$

where N is the number of design points, k – the number of variables in the approximate model, y_i – the simulation value, $\hat{y}$ – the predicted value, and $\overline{y}$ – the average of the simulated values.

Table 2 shows the final predicted values of the approximate model. The regression coefficients of training, test, validation, and overall model developed using RBFNN are shown in fig. 7. The value on the X-axis is the simulated value. The value on the Y-axis is the predicted value of the approximate model by the developed RBFNN. The high regression value reveals that the predicted values are substantially close to the simulated values for all data sets, which is an indication of the successful development of the RBFNN model. The best performance validation is obtained at the 6th iterations as shown in fig. 8. Equatiions (8) and (9) show that the value of R^2 is calculated to be 0.983, and the value of R^2_{adj} is 0.981. The fitting effect of the approximate model is satisfactory. The optimal value for the response f is 4.623 m/s. The optimal combination of parameters is L_1 = 340 mm, L_2 = 119 mm, and α = 62°.

Analysis of optimization

Table 3 shows the flow distribution before and after optimization. Excessive flow in the central outlet is distributed to the left and right outlets after optimization. The flow rate at the central outlet was reduced by 9.93%, the flow rate at the left outlet was increased by 3.90%, and the flow at the right outlet was increased by 4.16%.

Table 3. Flow distribution before and after optimization

	Before [%]	After [%]
Left outlet	19.44	23.34
Central outlet	38.56	28.63
Right outlet	20.00	24.16
Driver's side outlet	10.96	11.86
Passenger's side outlet	11.04	12.01

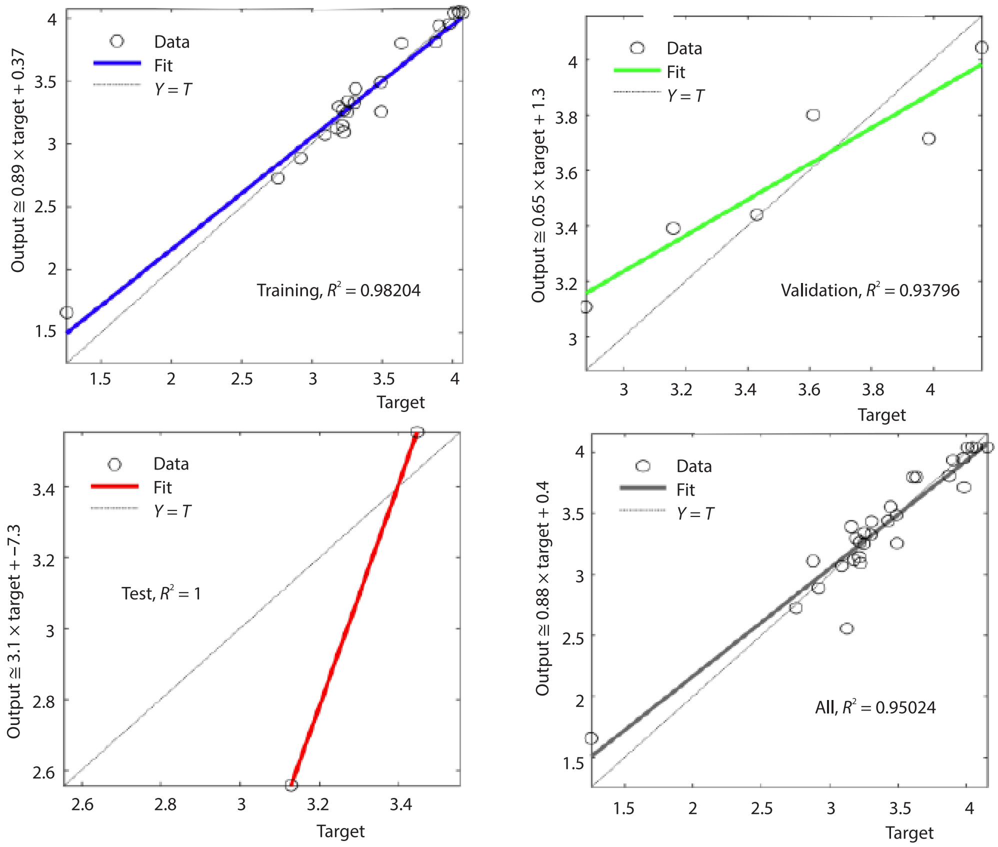

Figure 7. Regression coefficients of training, test, validation, and overall model

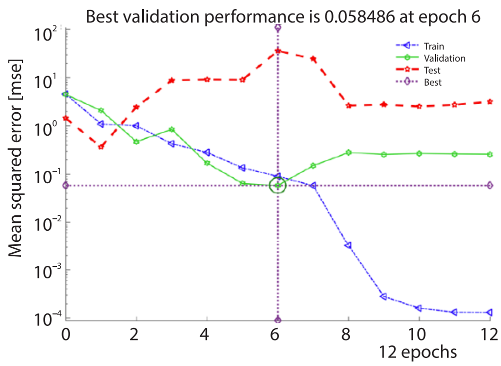

Figure 8. Best performance validation

Figure 9 shows the streamline distribution of the front windshield. The streamlines in the *A* and *A′* areas are relatively concentrated before optimization, thus, both areas can achieve an improved defrosting effect. Streamlines are absent in the lower left and right corners of thee *B* area, thus achieving poor defrosting effect. The streamlines completely cover the *A*, *A′*, and *B* areas after optimization, and the defrosting effect is improved.

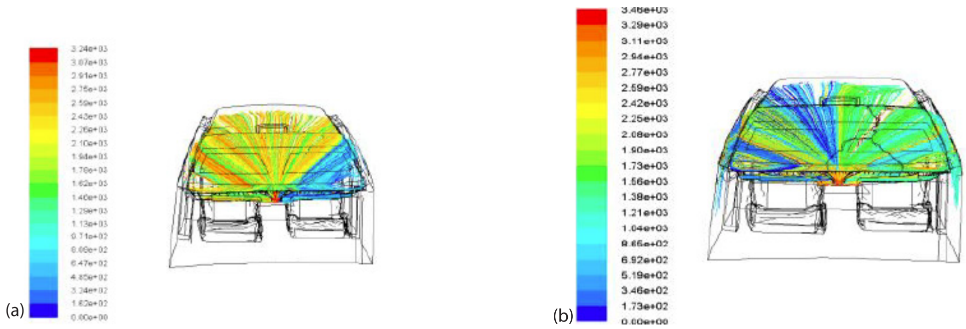

Figure 9. Steady-state streamline distribution; (a) before optimization and (b) after optimization

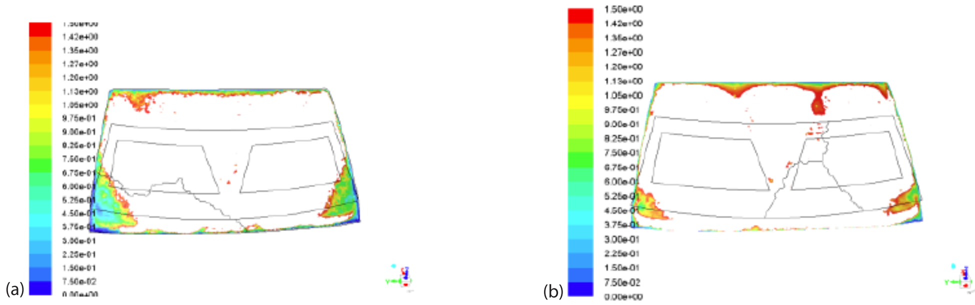

Figure 10. Steady-state air-flow velocity near the wall; (a) before optimization and (b) after optimization

Figure 10 shows the steady-state air-flow velocity. The white area means that the air-flow velocity is larger than 1.5 m/s and demonstrates an improved defrosting effect. The defrosting effect of the *A* and *A′* areas is remarkable before the optimization. The lower left and right corners of the *B* area have poor defrosting effects and are called defrosting dead corners. The defrosting dead corner accounts for approximately 20% of the *B* area. The defrosting dead corner is reduced from approximately 20-5% after optimization, and the defrosting effect is improved. This finding is consistent with the conclusions drawn in fig. 9.

Experimental verification

Verification of the frost layer melting effect

In the experiment, the test instruments include the Burke Porter Group Company drum test stand, spray gun, thermometer, engine tachometer, stopwatch, anemometer, voltmeter and camera. The environmental temperature is –18 °C ±3 °C, and the horizontal component of air velocity is less than 2.2 m/s. First, the test vehicle enters the low temperature chamber and needs to be parked for at least 10 hours. Then, the spray gun sprays water on the outer surface of the windshield to form a uniform ice layer. Spray velocity is 0.044 g/cm^2, the nozzle is 200~250 mm away from the glass surface, whose direction is perpendicular to the windshield. After the formation of uniform ice, the car still has to be parked in the low temperature chamber for 30-40 minutes. Then start the engine and open the defrost system at the same time, which means the defrost test begin. The test personnel recorded the defrost status every 5 minutes and took photos. Figure 11 compares the simulation results with the experimental results.

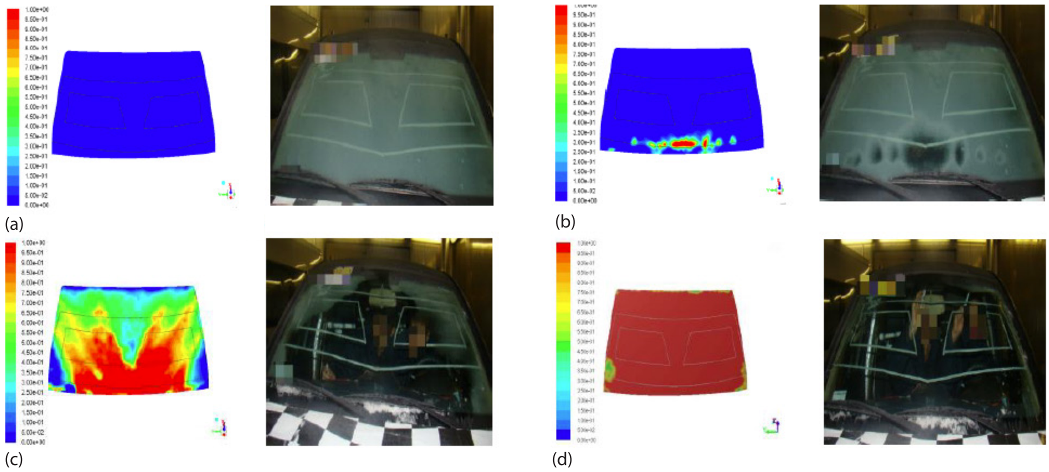

Figure 11. Frost melting effect; (a) 0, (b) 10, (c) 20, and (d) 25 minutes

The frost layer began to melt in 10 minutes. The defrosting area in *A* area reached 80% at 20 minutes, and the defrosting area in *A′* area reached 65%. The frost layers in *A*, *A′*, and *B* areas were all melted at 25 minutes, and the defrosting work was almost completed. Comparing the simulation and the experimental results, the position of the initial melting is the same, but the experimental melting area is slightly larger than the simulation. Figutre 12 shows the variation of the outlet air temperature per second. From 0-12 minutes, the inlet air temperature of the vehicle increases from –18 °C to approximate 10 °C. Early experiments reveal that the internal temperature of the front windshield increased, but the heat exchange between the glass and frost layer is not obvious. From 10-25 minutes, there has been a significant difference between the internal and external temperature of the front windshield, and as time passes, the heat transfer becomes better. From 25-40 minutes, the air temperature has reached more than 30°, during which time the defrost efficiency is getting faster and faster. in the 40th minute, the frost layer on the front windshield had been completely removed.

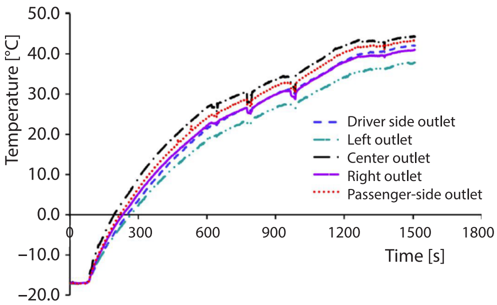

Figure 12. Air outlet temperature of each air outlet

Verification of air-flow temperature

The left and right outlets are structurally symmetrical. Thus, monitoring the air-flow temperature at the left and central outlets is necessary. Figure 13 compares the optimized simulation values with the experimental values. The results show that the experimental air-flow temperature is always higher than that of the simulation, thus, the experimental melting area is slightly larger than the simulated melting area. The air-flow is heated as it passes through the defrosting duct due to the generated heat during the experiment, while the simulation ignores the effects of convective heat transfer between the engine and the air-flow. The temperature difference gradually decreases with the increase in time, and the experimental melting area tends to be consistent with the simulated melting area. This result is in accordance with the conclusions drawn in fig. 11.

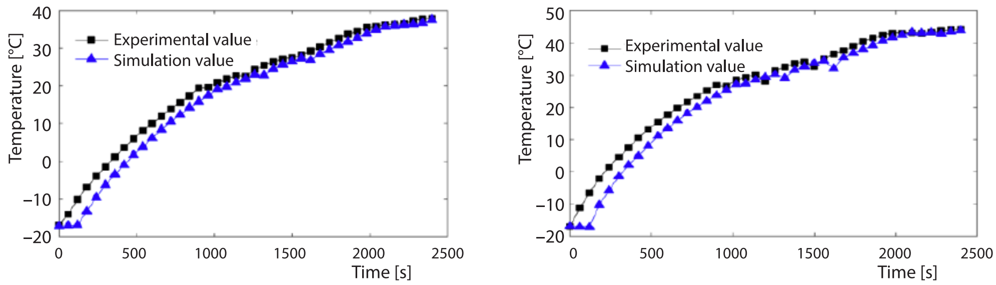

Figure 13. Air-flow temperature of the main outlet; (a) left outlet and (b) central outlet

Conclusions

A simulation analysis of the original automotive air conditioning system is conducted, and the simulation results revealed that the flow distribution is unreasonable. A structural topology scheme for additional horizontal grilles at the outlets is proposed to solve this problem. The following optimization parameters of the air conditioning are then determined: the length of the left outlet, L_1, the length of the central outlet, L_2, and the air-flow jet angle, α. The RBFNN is used to identify the optimal combination scheme of these parameters. The optimal combination of these parameters is $L_1 = 340$ mm, $L_2 = 119$ mm, and $\alpha = 62°$.

The flow of each outlet is rationally distributed after optimization: the flow rate of the central outlet is reduced by 9.93%, the flow rate of the left outlet is increased by 3.90%, and the flow rate of the right outlet is increased by 4.16%. The defrosting dead corner is reduced from 20-5%, and the defrosting performance is improved. The optimized model is verified by experiments. The defrosting area reached 80% at 20 minutes, and the defrosting area reached 65%. The frost layers were melted at 25 minutes. The experimental results are consistent with the simulation results, which verifies the effectiveness of the optimization model.

Acknowledgment

The authors gratefully acknowledge the financial support from Natural Science Foundation of Shanghai and National Natural Science Foundation of China (Grant No. 21ZR1425800 and 51577112).

Nomenclature

b_i – bias term
c_i – i^{th} Gaussian function center of the hidden layer
G_b – turbulent kinetic energy caused by buoyancy, [m^{2}s^{-2}]
G_k – turbulent kinetic energy caused by average velocity gradient, [m^{2}s^{-2}]
H – enthalpy, [J]
k – turbulent kinetic energy, [m^{2}s^{-2}]
N – number of design points
n, m – number of hidden layer nodes
T – temperature, [K]
u_i – velocity, [ms^{-1}]
$\vec{v}$ – fluid velocity, [ms^{-1}]
$\vec{v}_P$ – velocity of ice-water mixture, [ms^{-1}]
x_i, x_j – position vectors, [m]
x_p – p^{th} input sample
Y_M – contribution of compressible velocity turbulent pulsation expansion
y – predicted value
y_i – simulation value
$\overline{y}$ – average of the simulated values

Greek symbols

β – liquidus fraction
δ_i – variance of the i^{th} Gaussian function
ε – turbulent dissipation rate
μ_t – turbulent viscosity coefficient, [kgm^{-1}s^{-1}]
μ_1 – molecular viscosity
ρ – density, [kgm^{-3}]
σ_k, σ_ε – turbulent Prandtl number of turbulent kinetic energy and turbulent dissipation
ω_i – weight of the hidden layer to the output layer

References

[1] He, Z., *et al.*, Analysis and Optimization of Truck Windshield Defroster, *Applied Sciences*, *10* (2020), 16, 5671
[2] Huang, Y., *et al*., Optimal Energy-Efficient Predictive Controllers in Automotive Air-Conditioning/Refrigeration Systems, *Applied Energy*, *184* (2016), Dec., pp. 605-618
[3] Yang, Y., *et al*., Optimization of the Automotive Air Conditioning Strategy Based on the Study of Dewing Phenomenon and Defogging Progress, *Applied Thermal Engineering*, *169* (2020), 114932
[4] Duran, I. R., *et al*., Challenges, and Perspectives of Anti-Fogging Technology: Surface and Material Design, Fabrication Strategies, and Beyond, *Progress in Materials Science*, *99* (2019), Jan., pp. 106-186
[5] Guzej. M., Zachar M., The CFD Simulation of Defogging Effectivity in Automotive Headlamp, *Energies*, *12* (2019), 13, 609
[6] Kim, J. H., Rho, J. H., Design Optimization for Overhead Ventilation Duct System for a Train Using Computational Fluid Dynamics and Design of Experiment, Proceedings of the Institution of Mechanical Engineers, Part E: J*ournal of Process Mechanical Engineering*, *231* (2017), 5, pp. 914-929
[7] Ikeda, Y., *et al*., *Numerical Analysis of the Air-Flow on Windows from Defroster Nozzles*, JSAE paper, 1992, p. 924076
[8] Aroussi, A., Hassan, A., Vehicle Side-Window Defrosting and Demisting Process, *Proceedings*, EACC 2003 1st European Automotive CFD Conference, Bingen, Germany, 2003, pp. 155-163
[9] Swales, C., *et al*., Combining CAE and Experimental Techniques to Develop Optimal Defrost/Demist Performance in a Vehicle, *Proceedings*, SAE International 2004 SAE world Congress, Detroit, Mich., USA, 2004, 1506
[10] Kang, S. J., *et al*., Automobile Defrosting System Analysis Through a Full-Scale Model, International, *Journal of Automotive Technology*, *12* (2011), 1, pp. 39-44
[11] Karim, J., *et al*., *State of Knowledge and Current Challenges in Defrosting Automotive Windshields*, SAE Technical Paper Series, 2000, p. 980293
[12] Huang, T. M., *et al*., The Improved Research of the Defrosting of an Automobile Windshield, *Applied Mechanics and Materials*, *215* (2012), Nov., pp. 42-45
[13] Li, H., *et al.*, Numerical Simulation of Bus Windshield Based on Heat Transfer with Impinging Jets, *Advanced Materials Research*, *774* (2013), Sept., pp. 284-289
[14] Yang, Z., *et al*., Prediction and Optimization of Aerodynamic Noise in an Automotive Air Conditioning Centrifugal Fan, *Journal of Central South University, 20* (2013), 5, pp. 1245-1253
[15] Cho, S. K., *et al*., Design Optimization of Interior Permanent Magnet Synchronous Motor for Electric Compressors of Air-Conditioning Systems Mounted on EVs and HEV, *IEEE Transactions on Magnetics*, *54* (2018), 11, pp. 1-5
[16] Atuanya, C. U., *et al.*, Predicting the Mechanical Properties of Date Palm Wood Fibre-Recycled Low Density Polyethylene Composite Using Artificial Neural Network, *International Journal of Mechanical and Materials Engineering*, *1* (2014), Aug., p. 7
[17] Selvan, S. S., *et al*., Comparison of Response Surface Methodology (RSM) and Artificial Neural Network (ANN) in Optimization of Aegle Marmelos Oil Extraction for Biodiesel Production, *Arabian Journal for Science and Engineering*, *43* (2018), 11, pp. 6119-6131
[18] Esonye, C., *et al*., Optimization of Methyl Ester Production from Prunus Amygdalus Seed Oil Using Response Surface Methodology and Artificial Neural Networks, *Renewable Energy*, *130* (2019), Jan., pp. 61-72
[19] Hosoz, M., Ertunc, H. M., Artificial Neural Network Analysis of an Automobile Air Conditioning System, *Energy Conversion and Management*, *47* (2006), 11-12, pp. 1574-1587
[20] Giannetti, N., *et al*., Experimental Implementation of Artificial Neural Network for Cost Effective and Non-Intrusive Performance Estimation of Air Conditioning Systems, *Applied Thermal Engineering*, *181* (2020), 115985
[21] Ng B. C., *et al.*, Application of Multilayer Perceptron and Radial Basis Function Neural Network in Steady-state Modelling of Automotive Air Conditioning System, *Proceedings*, IEEE International Conference on Control System, Computing and Engineering, Penang, Malaysia, 2012, pp. 617-622
[22] Mirzaeinejad, H., Robust Predictive Control of Wheel Slip in Antilock Braking Systems Based on Radial Basis Function Neural Network, *Applied Soft Computing*, *70* (2018), Sept., pp. 318-329
[23] Rawaa, S., *et al*., A Comparison of Standard k-ε and Realizable k-ε Turbulence Models in Curved and Confluent Channels, *Environmental Fluid Mechanics*, *19* (2019), Oct., pp. 543-568

[24] Saidi, M. H., A New Approach in Developing Optimal Defrost/Demist Performance in a Passenger Car, *International Journal of Engineering*, *30* (2017), 7, pp. 1081-1089
[25] Koyuncu, H., Numerical Analysis of the Thermal Distribution of a Machinery Driver's Cab, Ph. D. thesis, Ankara Yıldırım Beyazıt Universitesi Fen Bilimleri Enstitusu, Ankara, Turkey, 2019
[26] Zou, Y., *et al*., Comparison of STAR-CCM+ and ANSYS FLUENT for Simulating Indoor Air-Flows, *Building Simulation*, *11* (2018), 1, pp. 165-174

Paper submitted: February 25, 2021
Paper revised: July 1, 2021
Paper accepted: July 6, 2021